UC Berkeley

UC Berkeley Previously Published Works

Title

Mechanisms of ultrafast GHz burst fs laser ablation

Permalink

https://escholarship.org/uc/item/0629c08c

Journal

Science Advances, 9(12)

ISSN

2375-2548

Authors

Park, Minok

Gu, Yueran

Mao, Xianglei

et al.

Publication Date

2023-03-24

DOI

10.1126/sciadv.adf6397

Peer reviewed

eScholarship.org Powered by the California Digital Library
University of California

APPLIED PHYSICS

Mechanisms of ultrafast GHz burst fs laser ablation

Minok Park[1,2,3], Yueran Gu[1,3], Xianglei Mao[1], Costas P. Grigoropoulos[2,3]*, Vassilia Zorba[1,3]*

Copyright © 2023 The Authors, some rights reserved; exclusive licensee American Association for the Advancement of Science. No claim to original U.S. Government Works. Distributed under a Creative Commons Attribution NonCommercial License 4.0 (CC BY-NC).

Gigahertz (GHz) femtosecond (fs) lasers have opened possibilities for enhancing and controlling the laser machining quality to engineer the physicochemical properties of materials. However, fundamental understanding of laser-material interactions by GHz fs laser has remained unsolved due to the complexity of associated ablation dynamics. Here, we study the ablation dynamics of copper (Cu) by GHz fs bursts using in situ multimodal diagnostics, time-resolved scattering imaging, emission imaging, and emission spectroscopy. A combination of probing techniques reveals that GHz fs bursts rapidly remove molten Cu from the irradiated spot due to the recoil pressure exerted by following fs pulses. Material ejection essentially stops right after the burst irradiation due to the limited amount of remnant matter, combined with the suppressed heat conduction into the target material. Our work provides insights into the complex ablation mechanisms incurred by GHz fs bursts, which are critical in selecting optimal laser conditions in cross-cutting processing, micro/nano-fabrication, and spectroscopy applications.

INTRODUCTION

Laser ablation, the process of material removal from a surface through its interaction with a high power laser, plays a pivotal role in many research areas and applications, including energy harvesting and storage (*1*, *2*), biomedicine (*3*, *4*), photonics (*5*–*7*), optoelectronics (*8*), and spectroscopy (*9*, *10*). These capabilities are enabled by unique laser attributes offering a direct, one-step, and chemical-free pathway for material machining, processing, fabrication, and ablation sampling (*11*, *12*). Of particular interest is ultrafast femtosecond (fs) laser ablation wherein deposition of the incident energy occurs extremely fast, leading to rapid phase change of the target material (*13*–*15*). Compared to longer pulses, one of the main advantages of fs laser ablation is the heat-affected zone suppression that helps achieve precise control of the ablation features (*1*, *6*, *7*, *16*).

Recently, the ability to generate bursts of fs laser pulses at gigahertz (GHz) frequencies has opened new possibilities for enhancing and controlling the laser machining quality. Ablation with GHz bursts of fs laser can lead to a mode that has been coined "ablation cooling," wherein the material removal is accompanied by limited heat accumulation (*17*). Characterization of the laser processed surfaces showed well-defined ablation features, suggesting diminished thermal effects in conjunction with augmented ablation efficiency (defined as the ablated volume per cumulative irradiated energy) by up to an order of magnitude. All of these are promising findings with potentially useful implications from the applications point of view.

The mechanisms of GHz fs laser ablation and ablation cooling remain to this date a topic of debate. Demonstrations have been largely limited to ex situ characterization of crater morphology and size (*18*, *19*) and numerical simulations (*17*, *20*), often with conflicting or incomplete findings. It has been proposed that the major driving force behind ablation cooling could be either evaporative removal or hydrodynamic motion of melt. Furthermore, the increased ablation efficiency has been ascribed to the rapid removal of preheated surface matter from the laser-matter interaction area by subsequent pulses in the GHz burst. However, the associated ablation dynamics must be experimentally validated. In situ characterization and diagnostic tools are required to directly probe the complex physicochemical dynamics and reactions (*11*, *12*) and thereby elucidate the ablation mechanisms by GHz fs laser bursts.

In this work, a suite of multimodal diagnostics (scattering imaging, emission imaging, and optical emission spectroscopy) was used to probe in real time the ablation dynamics. Ablation of copper (Cu) was examined under GHz fs laser pulse bursts and directly compared to single fs pulse ablation. The combination of in situ probing techniques in conjunction with ex situ surface morphology characterization revealed that GHz fs laser bursts result in fast removal of molten liquid material due to the recoil pressure exerted by the pulse train. As a result of the melt depletion, material removal stops after the burst irradiation. In contrast, single-pulse fs laser irradiation under the same total fluence, albeit at much higher peak power, leads to material ejection after its expiration due to persisting hydrodynamic instability effects. These findings provide direct insights into the dynamics and dominant mechanisms of GHz bust ablation with fs pulses.

RESULTS

Fig. 1A shows the optical system used to study the ablation mechanisms of Cu by single fs laser pulse (500-fs duration at 1030 nm) and GHz fs bursts (50 and 200 pulses at 1.28-GHz repetition rate) under atmospheric pressure. GHz pulse train profiles are shown in fig. S1. Time-resolved scattering and emission imaging were used to in situ probe particles, ejecta streaks, and plasma plumes using a continuous-wave (CW) probing laser, allowing visualization of both light-emitting and nonemitting species (inset, Fig. 1A). Furthermore, optical emission spectra were acquired to correlate the ejection dynamics with plasma chemistry. A detailed description of the experimental system is given in Materials and Method, while information on the Mie theory modeling (*21*) used to

[1]Laser Technologies Group, Energy Technologies Area, Lawrence Berkeley National Laboratory, Berkeley, CA 94720, USA. [2]Laser Thermal Laboratory, Department of Mechanical Engineering, University of California at Berkeley, Berkeley, CA 94720-1740, USA. [3]Department of Mechanical Engineering, University of California at Berkeley, Berkeley, CA 94720-1740, USA.
*Corresponding author. Email: cgrigoro@berkeley.edu (C.P.G.); vzorba@lbl.gov (V. Z.)

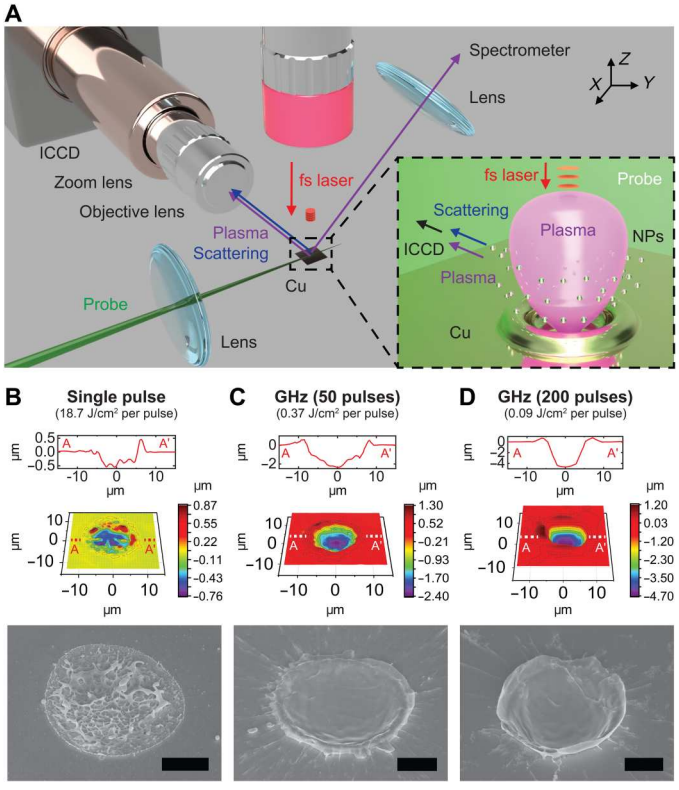

Fig. 1. Experimental system and morphological comparison of craters. (**A**) Optical setup for time-resolved scattering and emission imaging of GHz burst ablation dynamics with the ICCD camera. The 500-fs laser at 1030 nm was focused on the sample in the normal direction. A 532-nm CW probe laser was used for scattering imaging. Plasma-induced self-emission was used for imaging in the 500- to 930-nm spectral range without the probe laser. Ablation features at a total fluence of 18.7 J/cm^2 characterized by WLI (top) and SEM (bottom) for (**B**) single-pulse fs laser, (**C**) GHz burst with 50 pulses, and (**D**) GHz burst with 200 pulses, respectively. Black scale bars, 5 μm.

design the scattering imaging system is included in figs. S2 and S3 (*22*, *23*).

A constant laser fluence was used to directly compare the dynamics of fs GHz burst and single-pulse ablation. We used three total fluences (3.7, 18.7, and 29.8 J/cm^2) as summarized in table S1. Results at a total fluence of 18.7 J/cm^2 are shown in the main manuscript, while the rest are presented in the Supplementary Materials.

Figure 1 (B to D), fig. S4, and table S2 show ex situ ablation crater morphology characterization by white light interferometry (WLI) and scanning electron microscopy (SEM), for single fs pulse, GHz burst of 50 pulses, and GHz burst of 200 pulses, for the same total fluence of 18.7 J/cm^2. For single-pulse irradiation (Fig. 1B), the pristine Cu surface was ablated to a maximum depth of 500 nm (57.5-μm^3 ablated volume). Irregular resolidified structures appeared on the irradiated spot. However, GHz bursts of 50 pulses (0.37 J/cm^2 per pulse) and 200 pulses (0.09 J/cm^2 per pulse) produced maximum crater recesses of 2 μm (172.1 μm^3) and 4.5 μm (582.6 μm^3) below the original specimen surface (Fig. 1, C and D). Hence, the ablation efficiency by GHz bursts is improved by 3 to 10 times compared to single-pulse irradiation under the same total fluence. Protruding rims marked the edge of the craters and droplet fingers shot in the outward radial direction.

Shown in Fig. 2 are time-resolved emission images, emission spectra, and scattering images that capture the ablation dynamics by a single-pulse fs laser at 18.7 J/cm^2. Emission and scattering images for single-pulse ablation under different laser fluences (3.7 and 29.8 J/cm^2) are presented in figs. S5 to S7. After single-pulse irradiation, Cu plasmas are observed for approximately 30 ns (Fig. 2A). Figure 2B shows time-resolved emission spectra in the early stages of the laser-matter interaction, where the prominent atomic Cu lines (*24*) at 510.55, 515.32, and 521.82 nm are resolved. Note that emission near 515 nm at 0-ns delay is due to second-harmonic generation of the fundamental wavelength (1030 nm) from the Cu surface (*25*).

Scattering images reveal two different particle types ejected from the substrate: (i) particles released from 0- to 200-ns delay and (ii) particles ejected between 300-ns to 4-μs delay, as marked in Fig. 2C. The first type of particles has a 350-m/s ejection velocity (calculated from the green bars in Fig. 2C) in a vertical direction. Moreover, on the basis of Mie theory modeling in fig. S3 (*21*), particle sizes can be estimated because the relative intensity of the side-scattered light becomes weaker as the particle diameter decreases. Considering that a particle probed in the scattering image (yellow box, Fig. 2C) has a 2 μm diameter, ejected particles that make up the streak lines and silhouettes with weaker scattered light intensities are likely of the order of hundreds of nanometers in size. Hence, we assigned them as particles "A."

Previous work reported vertical ejection of nanoparticles (NPs) with velocities of 200 m/s under single-pulse fs laser irradiation and suggested that they would be generated via spallation due to ultrafast thermodynamic phase changes (*23*, *26*, *27*). Likewise, taking in account (i) the ablation depth of 500 nm (Fig. 1B), (ii) rapid ejection speed of 350 m/s, (iii) size of <1 μm, and (iv) direction of flight, particles A are likely expelled from the top surface of the bulk Cu via spallation.

Particles "B" were observed for higher laser fluences of 18.7 and 29.8 J/cm^2 in the scattering images (pink arrows in Fig. 2C and fig. S7). Their speeds are in the range of 27 to 180 m/s without a consistent directionality of flight. Particles B continued to be ejected over 4 μs (Fig. 2C and fig. S7D), while they were rarely detected under lower laser fluence of 3.7 J/cm^2 (fig. S6).

Although the incident light is deposited instantaneously, melting is formed at later times due to the coupling of the absorbed energy to the lattice system and the heat conduction into the bulk. Moreover, hydrodynamic instabilities on the liquid phase can be developed due to transient disturbances by evaporation and plasma expansion, leading to the ejection of droplets and liquid jets (*11*, *12*). The scattering images (Fig. 2C and red boxes in fig. S7) revealed that the expulsion of B particles is triggered by such mechanisms. This is consistent with the appearance of resolidified remnant morphology on the irradiated spot (Fig. 1B and fig. S4A).

Figure 3 shows time-resolved emission imaging and spectroscopy, along with scattering images of ablated plumes induced by GHz bursts composed of 50 pulses (38-ns dwell time) at a total laser fluence of 18.7 (0.37 J/cm^2 per pulse). Emission and scattering images for different total laser fluences (3.7 and 29.8 J/cm^2) are presented in figs. S8 to S10.

Figure 3A shows spherically shaped Cu plasmas for a period of 30 ns. The corresponding emission signals for the early stages of

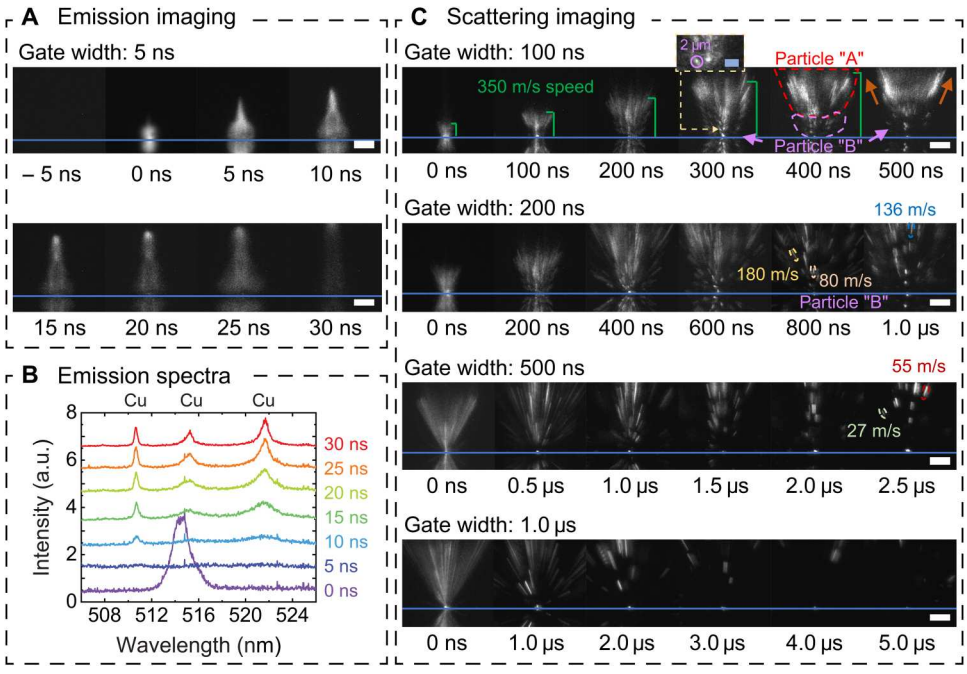

Fig. 2. Single-pulse fs laser irradiation. Time-resolved (**A**) emission imaging, (**B**) optical emission spectroscopy, and (**C**) scattering imaging showing the ablation dynamics at a fluence of 18.7 J/cm^2, across different time scales. a.u., arbitrary units. Scattering images were acquired for varying ICCD gate widths of 100 ns, 200 ns, 500 ns, and 1 μs, respectively. The blue lines in these images represent the Cu target surface, and images below the lines are mirror reflections from the polished Cu surface. White scale bars, 50 μm; blue scale bars, 10 μm.

expansion are shown in Fig. 3B. After the initial expansion of the plasma plumes, particles were released within 200 ns at a grazing angle with a speed of 130 m/s (calculated from green arrows, Fig. 3C). Their sizes are estimated to be in the order of hundreds of nanometers, using the methodology discussed in Fig. 2.

Unexpectedly, we were not able to detect ejecta at the center of the laser-matter interaction zone after 200 ns, and the target surface was not further ablated throughout the temporal range studied, up to 5-μs delay (pink arrows, Fig. 3C). Similar observations were made at a higher fluence of 29.8 J/cm^2 (0.6 J/cm^2 per pulse; fig. S10). Note that particles whose streak line trajectories are visible in the scattering images of Fig. 3C were already released before the 200-ns delay as the intensified charged coupled device (ICCD) gate opens at that time and till 300 ns. This ablation behavior is distinctly different from the single-pulse ablation images in Fig. 2.

On the basis of these observations, we anticipate two coupled contributing mechanisms for the observed material ejection: (i) vaporization of materials at the center region and (ii) ejection of liquid from the molten pool edge driven by fast radially outward fluidic motion. This flow is due to the recoil pressure exerted by vaporization [i.e., (i)]. Whereas Cu NPs are expelled from the edge of the molten pool with 130-m/s speed [i.e., (ii)], a limited amount of liquid is left to freeze on the crater surface, as verified by the cross-sectional SEM image (fig. S4B).

Moreover, in Fig. 1C, we did not observe evidence of irregularly resolidified surface morphologies on the irradiated spot akin to those formed upon single-pulse irradiation (Fig. 1B). Accordingly, there was no visual evidence of hydrodynamically induced material ejection in scattering images up to 5-μs delay for GHz burst of 50 pulses (Fig. 3C). This is in stark contrast to the images shown Fig. 2C for single fs pulse irradiation and the typical ablation behavior by ns laser (*28*) where the heat conducted to the target supports a deep melt pool and is therefore a major contributor to the continuing material ejection at much later times than the duration of the irradiated pulse. Last, materials that do not have sufficient momentum to escape are resolidified in the form of rims and droplet fingers (Fig. 1C).

Figure 4 shows time-resolved emission imaging, emission spectroscopy, and scattering imaging of ablation driven by GHz fs laser bursts of 200 pulses (155-ns dwell time) at a total fluence of 18.7 J/cm^2 (0.09 J/cm^2 per pulse). Emission and scattering images for different laser fluences (3.7 and 29.8 J/cm^2) are given in figs. S11 and S12. Figure 4 (A and B) shows faint plasma formation at the center of the laser-target interaction zone, as each pulse fluence in this experimental run is four times lower than in the 50 pulse GHz bursts. Ejecta were released within 300 ns into oblique directions with a 100-m/s ejection velocity (calculated from green bars, Fig. 4C). Similar to GHz burst with 50 pulses in Fig. 3, there was no evidence of particulate ejection at the center region from 300-ns to 5-μs gate delay. Ejecta shown in scattering images later than 300 ns were released from the surface before that time, suggesting that the irradiated spot cooled down to inhibit material removal as discussed in Fig. 3. The protruded rims shown in Fig. 1D are already visible around 300-ns gate delay (Fig. 4C and fig. S13).

A line of particles separated by 3 μm and an ejecta column of 3 μm in diameter could be distinguished at 1-μs gate delay (red box, Fig. 4C). Similar observations were made at a higher fluence of 29.8 J/cm^2 (0.15 J/cm^2 per pulse; fig. S12). Such formations were experimentally probed when the liquid-phase expulsion via recoil

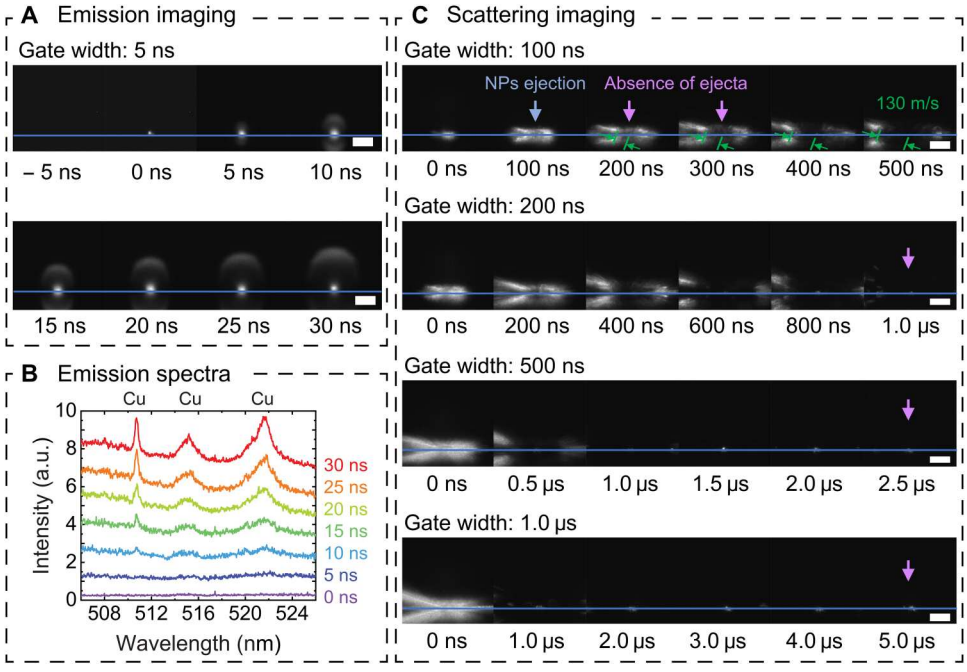

Fig. 3. GHz fs burst ablation with 50 pulses. Time-resolved (**A**) emission imaging, (**B**) optical emission spectroscopy, and (**C**) scattering imaging showing ablation dynamics and mechanisms at a fluence of 18.7 J/cm^2 (0.37 J/cm^2 per pulse, 38-ns dwell time). Scattering images were acquired for 100 ns, 200 ns, 500 ns, and 1 μs, respectively. The blue lines show the target Cu surface. White scale bars, 50 μm.

pressure contributed to the material removal in the case of liquid aluminum ablation under quasi-CW illumination (*22*).

Furthermore, two experimental conditions (0.07 J/cm^2 per pulse for 50 pulses versus 0.09 J/cm^2 per pulse for 200 pulses) were compared. In the first case (fig. S9), NPs were not produced but droplets of 5 μm in diameter were often ejected from the target surface. However, NPs and ejecta streaks were expelled from the surface for the latter case (Fig. 4C). Since the individual pulse fluence is similar for both cases, we can deduce that the first 50 pulses contribute to melting the Cu target because of heat accumulation, while the following 150 pulses trigger a succession of rapid liquid phase expulsion events in response to the exerted recoil forces. Material ejection was not observed after 300 ns because of the limited amount of liquid Cu remaining on the surface, given that molten traces on the surface were barely observed in the cross-sectional image (fig. S4C).

To further study the early ablation dynamics of Cu driven by GHz bursts of 50 and 200 pulses, we decreased the gate width to 50 ns and increased the image resolution using a higher magnification lens (20×), as shown in Fig. 5. GHz burst with 50 pulses (38-ns dwell time) caused the release of NPs at a grazing angle from the target surface (50-ns delay; Fig. 5A). However, as indicated with a yellow dome (100-ns delay; Fig. 5A), we were not able to probe ejecta within 12 μm in a radial direction. Since the ICCD gate opened from 100 to 150 ns, the absence of ejecta within this dome suggests that material ejection stopped within 100 ns from the beginning of the burst irradiation. Last, no ablation could be detected at later times (Figs. 5A and 3).

Conversely, the GHz burst with 200 pulses (155-ns irradiation time) drove different ablation dynamics compared to the GHz burst with 50 pulses (38-ns dwell time), as presented in Fig. 5. At 150-ns delay, ablated matter was ejected in a vertical direction (green arrows) with 100-m/s speed in short-lived (~100 ns) vertical columns with rippled surfaces (red boxes, Fig. 5B). Such disturbances were observed in laser-induced melting of metals due to hydrodynamic instabilities (*22*), which further supports the argument that ablation by GHz bursts with 200 pulses involves fluidic transport. In addition, the GHz burst with 200 pulses resulted in a longer ejection duration (<300 ns) from the surface than the GHz burst with 50 pulses (<100 ns). This is because it takes more time for the melt to escape due to the exerted lower pulse fluence and correspondingly weaker recoil pressure, in conjunction with a longer dwell time (i.e., deeper melting and enhanced mass removal; Fig. 1D).

The dimensionless Weber number ($We = \frac{\rho r V^2}{\sigma}$) describes the competition between kinetic energy and surface tension (*29*, *30*). Here, ρ is the density of liquid Cu (7900 kg/m^3) (*31*), V is the ejection speed (100 m/s), r is the radius of the streak (1.2 μm), and σ is the surface tension of liquid Cu (1.2 N/m) (*32*). The corresponding *We* number is 79 (>>4), indicating that the kinetic energy is sufficient to overcome the liquid Cu surface tension. Hence, vertically ejected liquid columns detached from the surface and then fragmented into particles (300 ns in Fig. 5B), as discussed in Fig. 4. Liquid matter lacking sufficient momentum resolidified to a cup-shaped surface.

Figure 6A shows the combined distance-time (R-t) plots of ejected material by single fs pulse (top trace) and GHz fs laser bursts under 50 and 200 pulses for the same total fluence (18.7 J/cm^2). For single-pulse irradiation, particles A were released with a velocity of 350 m/s, while particles B were ejected with random speeds <200 m/s. For a GHz burst with 50 pulses, NPs were expelled under 130-m/s ejection speed, while NPs and ejecta streaks were removed at 100-m/s velocity for a GHz burst with 200 pulses.

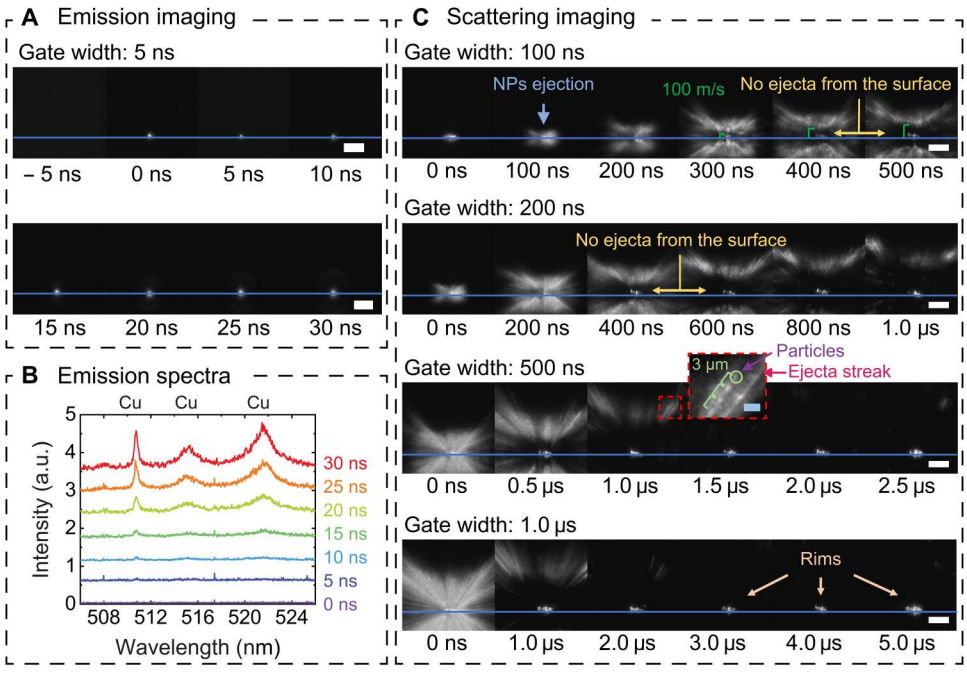

Fig. 4. GHz fs burst ablation with 200 pulses. Time-resolved (**A**) emission imaging, (**B**) optical emission spectroscopy, and (**C**) scattering imaging to investigate ablation dynamics by GHz fs laser with 200 pulses at a fluence of 18.7 J/cm^2 (0.09 J/cm^2 per pulse, 155 ns total irradiation time), across different time scales. Scattering images were captured for 100 ns, 200 ns, 500 ns, and 1 µs, respectively. The blue lines represent the target Cu surface. White scale bars, 50 µm; blue scale bars, 10 µm.

Figure 6 (B and C) summarizes the ablation dynamics of Cu by single-pulse fs laser and GHz fs laser bursts, based on the experimental results discussed in Figs. 2 to 5. Under single-pulse irradiation (Fig. 6B), particles A are produced due to spallation of the top skin-depth layer. Subsequent melting of underlying material generated particles B (>300 ns) via hydrodynamic instabilities. In cases of GHz bursts, preheated surface material by preceding pulses is rapidly removed from the surface by subsequent pulses (Fig. 6C). Accordingly, longer time ablation is prevented after burst irradiation due to the limited amount of remnant matter, combined with suppression of heat conduction into the target material.

This work provides direct confirmation of the different ablation mechanisms with GHz bursts compared to single-pulse irradiation under the same total fluence. We find that a higher fraction of the incident laser energy is carried away by the ejecta, while more material is ablated, and less heat is transported by conduction to the bulk of the target in the case of GHz bursts. The number of GHz burst pulses and pulse fluence determines the form of the ejecta and the duration of the ablation event. Per our observation, the mechanism of GHz burst ablation for the range of total fluence and number of pulses examined in this work is mainly driven by the action of recoil pressure on melt via subsequent laser pulses.

DISCUSSION

The ablation dynamics of Cu by single fs laser pulses and GHz bursts with 50 pulses and 200 pulses were investigated via in situ multimodal probing techniques. Single-pulse fs laser irradiation generated two types of particles with different ejection speeds at different time scales. GHz fs laser bursts incurred a succession of rapid ablation events ejecting NPs and ejecta streaks due to recoil pressure forces exerted on the molten pool by subsequent pulses, while farther material ejection at longer times could not be sustained due to the rapid cooling of the shallow remnant liquid phase. Ablation dynamics induced by GHz bursts depend on the tunable burst parameters, including the number of burst pulses, irradiation time, and pulse fluence. In all GHz ablation cases, plasma plumes were observed within 30 ns after the pulse. These findings contribute toward comprehensive understanding of ablation mechanisms by GHz fs bursts, which is critical in the selection of optimal GHz burst conditions for a variety of applications in laser processing, machining, printing, and laser plasma generation for spectroscopic diagnostics.

MATERIALS AND METHODS

Materials

Cu substrates of 0.5 mm thickness (one-side polished; purity, 99.99%; roughness, <10 nm; MTI Corporation) were used as target specimens. To ensure consistency and reproducibility, each measurement was performed on a fresh sample location.

Single-pulse fs laser and GHz bursts fs laser

A femtosecond laser (Tangor, Amplitude) that operates in single pulse or GHz burst modes (50 pulses and 200 pulses for a 1.28-GHz repetition rate) was used for this study. The corresponding GHz pulse train profiles measured with a fast photodiode (DET08C, Thorlabs) and an oscilloscope (MSO64, Tektronix) are presented in fig. S1. Fs laser pulses (500-fs pulse duration and 1030-nm wavelength) were focused via a 5× near-infrared objective lens (Mitutoyo) on the sample in the normal direction, yielding a 16-µm beam diameter.

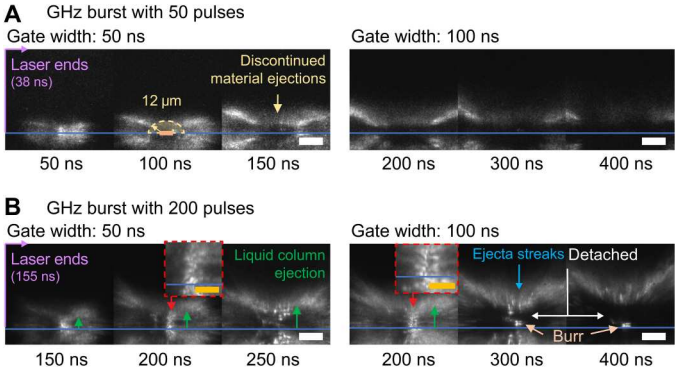

Fig. 5. Early dynamics of Cu ablation induced by GHz bursts. Time-resolved scattering images for (**A**) 50 pulses, and (**B**) 200 pulses were acquired for 50- and 100-ns gate width. The blue line indicates the target Cu surface. White scale bars, 25 μm; orange scale bars, 10 μm.

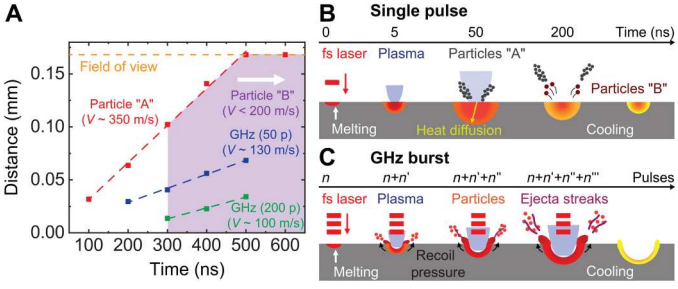

Fig. 6. Summary of ablation dynamics. (**A**) *R-t* plots of observed ejecta induced by single-pulse fs laser and GHz bursts. Experimental findings on the ablation dynamics by (**B**) single-pulse fs laser and (**C**) GHz fs lasers.

Time-resolved scattering imaging, emission imaging, and optical emission spectroscopy

Mie theory modeling provides information on the angular distribution of scattered light away from a spherical particle as a function of the particle diameter and the spectrally dependent complex refractive index (*21*). Since particles ejected from the target surface are likely to be in liquid state within a 5-μs temporal window after the initial release (see derivation in fig. S2), the complex refractive index of liquid Cu (n = 0.94 and k = 2.94 at 532 nm) (*33*) can be used for modeling purposes. As shown in fig. S3, collection of side scattering is preferable to avoid enhanced forward scattering by larger particles and the directly transmitted probing laser light. Hence, the CW probe laser was focused by a convex lens (f = 50 mm) at 90°, which is perpendicular to the detection angle, as depicted in Fig. 1A.

Moreover, the time-resolved scattering imaging system was established with 10× and 20× objective lenses (Mitutoyo), a 12× zoom lens (Navitar), an ICCD camera (PI-MAX2, Princeton Instruments), and a 532-nm CW probe laser (Laserglow Technologies). The 532-nm probing wavelength is selected upon examining the spectral dependence of the predicted angular scattering distributions shown in fig. S3. The optical power of the probe laser was fixed at 1.0 W to prevent ICCD pixel saturation.

Time-resolved emission imaging was accomplished on the same setup without the probing laser to analyze the plasma-induced optical emission from Cu in the 500- to 930-nm spectral range and was filtered by a bandpass filter (FESH0950, Thorlabs). Optical emission spectra were acquired to correlate ejection dynamics with plasma chemistry. Spectral optical emission was collected by two convex lenses and focused into an optical fiber coupled to a spectrometer (IsoPlane, Princeton Instruments) equipped with a separate ICCD camera (PI-MAX3, Princeton Instruments). The gate delay indicates the elapsed time from the beginning of the GHz pulse train till the commencement of the ICCD camera acquisition and the gate width represents the duration of the image acquisition.

Surface morphology characterization

Following laser irradiation, the sample surface morphology was characterized using WLI (NewView 6000, Zygo) and SEM.

Supplementary Materials

This PDF file includes:

Figs. S1 to S13
Tables S1 and S2
References

REFERENCES AND NOTES

1. S. C. Singh, M. ElKabbash, Z. Li, X. Li, B. Regmi, M. Madsen, S. A. Jalil, Z. Zhan, J. Zhang, C. Guo, Solar-trackable super-wicking black metal panel for photothermal water sanitation. *Nat. Sustain.* **3**, 938–946 (2020).
2. S. A. Jalil, B. Lai, M. ElKabbash, J. Zhang, E. M. Garcell, S. Singh, C. Guo, Spectral absorption control of femtosecond laser-treated metals and application in solar-thermal devices. *Light Sci. Appl.* **9**, 14 (2020).
3. R. Y. Siddiquie, A. Gaddam, A. Agrawal, S. S. Dimov, S. S. Joshi, Anti-biofouling properties of femtosecond laser-induced submicron topographies on elastomeric surfaces. *Langmuir* **36**, 5349–5358 (2020).
4. S. I. Kudryashov, L. V. Nguyen, D. A. Kirilenko, P. N. Brunkov, A. A. Rudenko, N. I. Busleev, A. L. Shakhmin, A. V. Semencha, R. A. Khmelnitsky, N. N. Melnik, I. N. Saraeva, A. A. Nastulyavichus, A. A. Ionin, E. R. Tolordava, Y. M. Romanova, Large-scale laser fabrication of antifouling silicon-surface nanosheet arrays via nanoplasmonic ablative self-organization in liquid CS2Tracked by a sulfur dopant. *ACS Appl. Nano Mater.* **1**, 2461–2468 (2018).
5. J.-M. Guay, A. Calà Lesina, G. Côté, M. Charron, D. Poitras, L. Ramunno, P. Berini, A. Weck, Laser-induced plasmonic colours on metals. *Nat. Commun.* **8**, 16095 (2017).
6. A. Y. Vorobyev, C. Guo, Colorizing metals with femtosecond laser pulses. *Appl. Phys. Lett.* **92**, 041914 (2008).
7. V. Zorba, E. Stratakis, M. Barberoglou, E. Spanakis, P. Tzanetakis, S. H. Anastasiadis, C. Fotakis, Biomimetic artificial surfaces quantitatively reproduce the water repellency of a lotus leaf. *Adv. Mater.* **20**, 4049–4054 (2008).
8. D. Paeng, J. H. Yoo, J. Yeo, D. Lee, E. Kim, S. H. Ko, C. P. Grigoropoulos, Low-cost facile fabrication of flexible transparent copper electrodes by nanosecond laser ablation. *Adv. Mater.* **27**, 2762–2767 (2015).
9. R. E. Russo, X. Mao, J. J. Gonzalez, V. Zorba, J. Yoo, Laser ablation in analytical chemistry. *Anal. Chem.* **85**, 6162–6177 (2013).
10. M. Boueri, M. Baudelet, J. Yu, X. Mao, S. S. Mao, R. Russo, Early stage expansion and time-resolved spectral emission of laser-induced plasma from polymer. *Appl. Surface Sci.* **255**, 9566–9571 (2009).
11. D. W. Bäuerle, *Laser Processing and Chemistry*. (Springer, ed. 4, 2011).
12. C. P. Grigoropoulos, *Transport in Laser Microfabrication: Fundamentals and Applications*. (Cambridge Univ. Press, 2009).
13. R. Fang, A. Vorobyev, C. Guo, Direct visualization of the complete evolution of femtosecond laser-induced surface structural dynamics of metals. *Light Sci. Appl.* **6**, e16256 (2017).
14. K. Sokolowski-Tinten, J. Bialkowski, A. Cavalleri, D. von der Linde, A. Oparin, J. Meyer-ter-Vehn, S. I. Anisimov, Transient states of matter during short pulse laser ablation. *Phys. Rev. Lett.* **81**, 224–227 (1998).
15. K. Sugioka, Y. Cheng, Ultrafast lasers—Reliable tools for advanced materials processing. *Light Sci. Appl.* **3**, e149 (2014).
16. B. N. Chichkov, C. Momma, S. Nolte, F. von Alvensleben, A. Tünnermann, Femtosecond, picosecond and nanosecond laser ablation of solids. *Appl. Phys. A* **63**, 109–115 (1996).

17. C. Kerse, H. Kalaycıoğlu, P. Elahi, B. Çetin, D. K. Kesim, Ö. Akçaalan, S. Yavaş, M. D. Aşık, B. Öktem, H. Hoogland, R. Holzwarth, F. Ö. Ilday, Ablation-cooled material removal with ultrafast bursts of pulses. *Nature* **537**, 84–88 (2016).
18. G. Bonamis, K. Mishchick, E. Audouard, C. Hönninger, E. Mottay, J. Lopez, I. Manek-Hönninger, High efficiency femtosecond laser ablation with gigahertz level bursts. *J. Laser Appl.* **31**, 022205 (2019).
19. K. Mishchik, G. Bonamis, J. Qiao, J. Lopez, E. Audouard, E. Mottay, C. Hönninger, I. Manek-Hönninger, High-efficiency femtosecond ablation of silicon with GHz repetition rate laser source. *Opt. Lett.* **44**, 2193–2196 (2019).
20. H. Matsumoto, Z. Lin, J. Kleinert, Ultrafast laser ablation of copper with ~GHz bursts. *Proc. SPIE* **10519**, (2018).
21. C. F. Bohren, D. R. Huffman, *Absorption and Scattering of Light by Small Particles* (Wiley, 1998).
22. M. Park, M. M. Balkey, X. Mao, C. P. Grigoropoulos, V. Zorba, Spatio-temporal ablation dynamics and plasma chemistry of aluminum induced by temporally modulated ytterbium fiber laser. *Appl. Phys. Lett.* **119**, 224103 (2021).
23. M. Park, J. Jeun, G. Han, C. P. Grigoropoulos, Time-resolved emission and scattering imaging of plume dynamics and nanoparticle ejection in femtosecond laser ablation of silver thin films. *Appl. Phys. Lett.* **116**, 234105 (2020).
24. A. G. Shenstone, C. R. Darwin, The first spectrum of copper (Cu I). *Philos. Trans. R. Soc. Lond A Math. Phys. Sci.* **241**, 297–322 (1948).
25. J. Hohlfeld, D. Grosenick, U. Conrad, E. Matthias, Femtosecond time-resolved reflection second-harmonic generation on polycrystalline copper. *Appl. Phys. A* **60**, 137–142 (1995).
26. C. Wu, L. V. Zhigilei, Microscopic mechanisms of laser spallation and ablation of metal targets from large-scale molecular dynamics simulations. *Appl. Phys. A* **114**, 11–32 (2014).
27. C. M. Rouleau, C. Y. Shih, C. Wu, L. V. Zhigilei, A. A. Puretzky, D. B. Geohegan, Nanoparticle generation and transport resulting from femtosecond laser ablation of ultrathin metal films: Time-resolved measurements and molecular dynamics simulations. *Appl. Phys. Lett.* **104**, 193106 (2014).
28. J. H. Yoo, S. H. Jeong, R. Greif, R. E. Russo, Explosive change in crater properties during high power nanosecond laser ablation of silicon. *J. Appl. Phys.* **88**, 1638–1649 (2000).
29. S. P. Lin, R. D. Reitz, Drop and spray formation from a liquid jet. *Annu. Rev. Fluid Mech.* **30**, 85–105 (1998).
30. W. van Hoeve, S. Gekle, J. H. Snoeijer, M. Versluis, M. P. Brenner, D. Lohse, Breakup of diminutive Rayleigh jets. *Phys. Fluids* **22**, 122003 (2010).
31. M. J. Assael, A. E. Kalyva, K. D. Antoniadis, R. M. Banish, I. Egry, J. Wu, E. Kaschnitz, W. A. Wakeham, Reference data for the density and viscosity of liquid copper and liquid tin. *J. Phys. Chem. Ref. Data Monogr.* **39**, 033105 (2010).
32. T. Matsumoto, H. Fujii, T. Ueda, M. Kamai, K. Nogi, Measurement of surface tension of molten copper using the free-fall oscillating drop method. *Meas. Sci. Technol.* **16**, 432–437 (2005).
33. J. C. Miller, Optical properties of liquid metals at high temperatures. *Philos. Mag.* **20**, 1115–1132 (1969).
34. K. C. Mills, B. J. Monaghan, B. J. Keene, Thermal conductivities of molten metals: Part 1 pure metals. *Int. Mater. Rev.* **41**, 209–242 (1996).
35. V. Y. Chekhovskoi, V. D. Tarasov, Y. V. Gusev, Calorific properties of liquid copper. *High Temp.* **38**, 394–399 (2000).

Acknowledgments: We thank Applied Spectra Inc. for use of one of their ICCD cameras. **Funding:** This work was supported by the U.S. Department of Energy, Office of Defense Nuclear Nonproliferation Research and Development under contract number DE-AC02-05CH11231. C.P.G. acknowledges support by the NSF under Grant CBET-2126682. **Author contributions:** Conceptualization: M.P., C.P.G., and V.Z. Methodology: M.P., Y.G., and X.M. Investigation: M.P., Y.G., and X.M. Supervision: C.P.G. and V.Z. Writing–original draft: M.P., C.P.G., and V.Z. Writing–review and editing: M.P., C.P.G., and V.Z. **Competing interests:** The authors declare that they have no competing interests. **Data and materials availability:** All data needed to evaluate the conclusions in the paper are present in the paper and/or the Supplementary Materials.

Submitted 3 November 2022
Accepted 21 February 2023
Published 22 March 2023
10.1126/sciadv.adf6397